P-ISSN: 2987-7261
E-ISSN: 2987-7253

Jurnal Riset Ilmu Teknik
Journal homepage: https://jurnaljepip.com/index.php/jurit
Vol 4, No. 2, pp. 52-63, 2026
DOI: doi.org/10.59976/jurit.v4i2.367

Performance of Pineapple Leaf Fiber-Based Composite Bearing Thermofluids in Evaporative Cooling: A CFD Study with the Taguchi L9 Design

Joel Mangasi Tua Purba[1]*, Ayu Zahra Chandrasari[2]
Universitas Widyatama, Bandung, Indonesia
*Corresponding Author: joel.tua@widyatama.ac.id

ABSTRACT

The use of synthetic materials in evaporative cooling pads has prompted the exploration of pineapple leaf fiber (PALF)-based composites; however, the sensitivity of their thermophysical properties regarding thermofluid performance remains unquantified. This study aims to examine the sensitivity of material density, porosity, and thermal conductivity to temperature drop (ΔT), cooling effectiveness, and pressure drop (ΔP). Steady-state, fully wetted, homogeneous porous zone Computational Fluid Dynamics (CFD) simulations were conducted using a Taguchi L9 orthogonal array (3 factors × 3 levels). Inlet air conditions were set at a temperature of 21°C, a relative humidity of 79.2%, and a velocity of 1 m/s. A "larger-the-better" Signal-to-Noise (S/N) ratio analysis was applied to evaluate factor sensitivity rankings across the tested levels. Based on delta S/N values, porosity ranked highest in sensitivity regarding its influence on ΔT, followed by thermal conductivity and density. Combination S5 (porosity 0.9198, density 953.3 kg/m^3, and thermal conductivity 0.0489 W/m·K) yielded a ΔT of 0.147°C, cooling effectiveness of 5.627%, and ΔP of 0.172 Pa. The theoretical temperature drop is limited by the inlet air's wet-bulb temperature. This study did not involve physical sample fabrication, testing of absorption or durability, or direct experimental comparison with commercial pads. The results present numerical sensitivity trends under the tested simulation conditions to serve as a guide for pore architecture design, rather than a physical validation of replacing commercial materials.

Keywords: *Computational Fluid Dynamics, Porous Media, Taguchi Method, Evaporative Cooling, Pineapple Leaf Fiber.*

Manuscript received 02 July 2026; revised 19 August 2026 accepted 28 August. 2026.

INTRODUCTION

The need for room temperature conditioning continuously encourages high energy consumption in the building sector [1]. So far, air conditioning (AC) based on refrigerant steam compression cycles has become the main technology [2]. As an energy-efficient alternative, direct evaporative cooling (DEC) technology is present to utilize the conversion of sensitive heat into evaporative energy (latent heat) air-water [3]. The operational performance of the DEC system is measured through several key design indicators, such as wet-bulb effectiveness, pressure drop which affects fan power consumption, water consumption, and temperature drop (ΔT) [3], [4]. Despite being energy efficient, the application of DEC in tropical regions is often hampered by high free relative humidity (RH) conditions, which limit the saturation limit of air evaporation [4].

The heart of the DEC system is the cooling pad. Commercial pads made of corrugated cellulose paper are currently commonly used [6]. However, extreme wet-dry cycles often trigger biological degradation [5]. In addition, the environmental footprint of commercial polymer/paper manufacturing and chemical consumables in the industry in general demands the search for alternative raw materials that are more environmentally friendly and economical [7]. Utilizing local biomass such as pineapple leaf fiber (PALF) is a potential motivation for the synthesis of synthetic materials [8]–[10]. In contrast to single fiber or bulk pads, natural fiber-based composites such as in polymer-PALF composite studies have specific thermomechanical characteristics, such as size stability and certain effective thermal conductivity [11], [12]. Although the properties of the polymer composite literature do not directly reflect the water absorption of wet pads, their density, effective porosity, and thermal conductivity values can be transferred into macroscopic numerical modeling as an approach to the parameters of early thermofluid architecture.

Previous studies have tested a variety of natural fibers, such as palm fiber [4] and various other porous media, for thermofluid applications. On the other hand, Computational Fluid Dynamics (CFD) has proven to be robust in modeling heat transfer and coupled mass in porous zones [13], [14], [16], [24], measuring flow resistance [25], [30], and simulating phase-change-based heat transfer rates [15], [31]. However, no studies have systematically integrated the variation in thermophysical properties of PALF composites into DEC CFD simulations. The literature comparison matrix (Table 1) clarifies the novelty of this study compared to previous studies.

Table 1. State of the Art Matrix and Research Gaps

Researcher & Reference	Cooling Material	Method	Key Variables/Responses	Research Gap
Patel et al. [3]	General	Overview	Effectiveness, Cooling Capacity	No specific data on the properties of the new fiber
Almaneea et al. [4]	Palm Tree Waste	Experiments	T/RH, Speed, ΔT	Macro studies, not evaluating specific pore architecture
Al-damook et al. [13]	Numerically Porous Zones	CFDs	Porosity, Heat Transfer	Not for evaporative cooling applications
Gan et al. [27]; Marykovskiy et al. [25]	Generic Porous Media	Experiments/CFDs	Pressure Loss, Forchheimer Resistance	Does not correlate water-air latent heat transfer
This Study	PALF-Based Composites	CFD & Taguchi L9	Density, Porosity, Thermal Conductivity→ΔT, Effectiveness, ΔP	CFD-Taguchi parametric integration for the thermophysical properties of PALF in DEC

Based on the roadmap, the main unanswered research question is the extent to which the influence of pore architectural variations (density, porosity, and thermal conductivity) based on PALF composites affects the cooling performance and aerodynamic resistance of the system. Therefore, this study aims to: (1) evaluate the temperature drop (ΔT), cooling effectiveness, and pressure loss (ΔP) in PALF composite bearings, (2) rank the sensitivity of such thermophysical factors, and (3) formulate the most numerically optimal combination of design levels.

To efficiently achieve this goal, the experimental design (DoE) of the Taguchi L9 orthogonal matrix was integrated into the CFD modeling. The use of Taguchi has been shown to be reliable in the optimization of complex multidimensional parameters in various manufacturing and thermal fields [18]–[20], [34]. It should be emphasized that these simulations are limited to a single test scenario i.e., an inlet temperature of 21∘C, RH 79.2%, and a velocity of 1 m/s that represent specific humid air conditions in which the potential for water evaporation is critically depressed. The resulting conclusions are numerical potentials and specifically apply only to the range of property level and thermodynamic boundary conditions tested, with no intention of generalizing the performance of its physical pad to all tropical climate scenarios.

METHOD

Geometry Configuration and Net Independence

Macroscopic porous media numerical modeling was performed to analyze the thermofluid performance of pineapple leaf fiber-based composite evaporative cooling pads (PALF). The 3D geometry of the computing domain and the test duct is explicitly shown in Figure 1. A porous bearing measuring 100 mm×1830 mm×width 650 mm) is placed in the test chamber with an identical cross-section (Blockage Ratio 100%) to prevent bypass flow around the media. The computing domain is extended upstream (upstream length, Lhulu=1000 mm) to ensure that the inflow of incoming air is fully developed flow, as well as downstream length, Lhilir=2000 mm to prevent the effect of recirculation/backflow on the output field.

The boundary conditions applied include: Velocity Inlet at the inlet domain (v=1 m/s, T=21∘C, RH=79.2%), Pressure Outlet at the output field (Pgauge=0 Pa), and No-Slip Adiabatic Wallat the entire boundary of the test aisle wall. Output parameter data retrieval including output temperature (Tout), output relative humidity (RHout), and pressure difference (ΔP=Pin−Pout) were extracted precisely at the cross-sectional plane of the bearing output (x=100 mm) using the mass-weighted average method to ensure an accurate representation of the flux mean value.

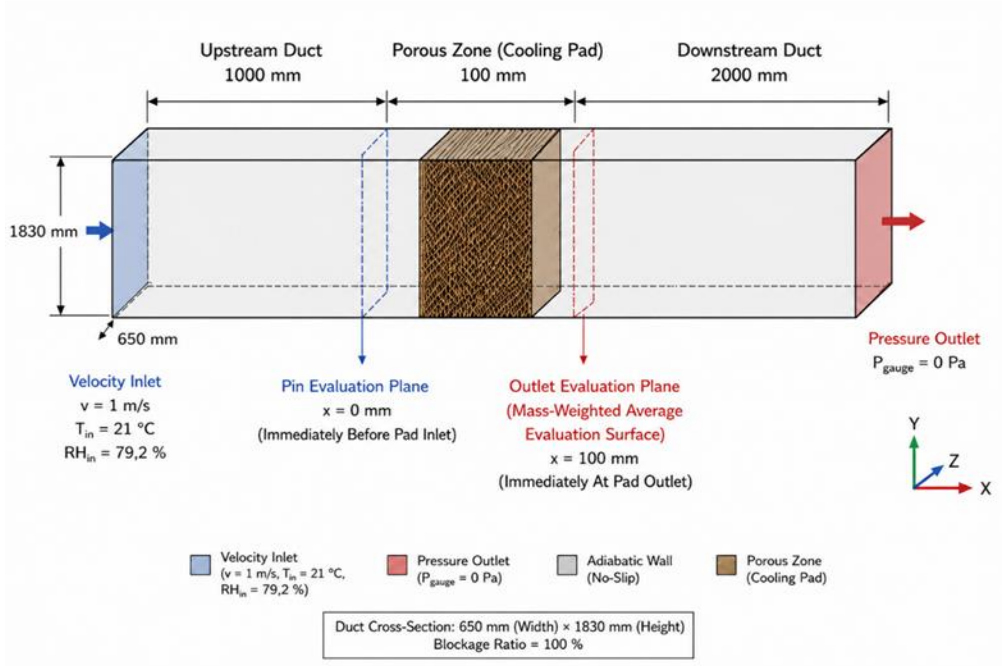

Figure 1. 3D schematic of the evaporative cooling test duct computing domain: upstream-downstream dimensions, boundary conditions (Inlet, Outlet, Wall), and cross-sectional field markers of mass-weighted average data evaluation (Tout,RHout,ΔP).

Domain dyskritisty uses the Hex-Dominant method with a near-wall prism layer to maintain the dimensionless value of the wall (y+≈1) [13], [16]. The qualification of spatial dyskritisation and grid uncertainty was evaluated quantitatively using the ASME V&V 20 standard-based Grid Convergence Index (GCI) method and the Roache criterion [35] at three levels of mesh density: Coarse (N3=187.102), Medium (N2=360.087), and Fine (N1=728.824). The entire mesh level met the high mesh quality criteria with orthogonal quality>0.82 and skewness <0.15. Convergence evaluation was carried out simultaneously on two key thermofluid responses: mass average output temperature (Tout) and pressure loss (ΔP).

The effective net purification ratio between the medium-fine lattices is calculated as r21=(N1/N2)$^{1/3=1.265.}$ The pseudo-relative error (ea) and the GCI uncertainty index are formulated in Equations (1) and (2).

$$e_{a,21} = \left|\frac{f_1 - f_2}{f_1}\right| \times 100\% \quad (1)$$

$$GCI_{21} = \frac{F_s \cdot e_{a,21}}{r_{21}^{p} - 1} \quad (2)$$

where F1 and F2 are the response values on fine and medium nets, p=2 is the solver's formal order of precision, and Fs=1.25 is the safety factor for the three-level study of the net. The results of the GCI calculation are presented in Table 2.

Table 2. Net Independence Testing and GCI Uncertainty Analysis (ASME V&V 20)

Net Levels	Number of Elements (N)	Output Temperature, Tout (K)	Galat ea,21(All)	GCI21(All)	Pressure Loss, ΔP (Pa)	Error ea,21(ΔP)	GCI21(ΔP)
Coarse (N3)	187.102	294,321	-	-	0,1742	-	-
Intermediate (N2)	360.087	294,003	0,108%	-	0,1724	1,033%	-
Smooth (N1)	728.824	293,959	0,015%	0,031%	0,1720	0,233%	0,485%

The GCI21 values for both responses were recorded well below the 1% uncertainty threshold (0.031% for Tout and 0.485% for ΔP), confirming that the numerical solution had reached convergence and was within the asymptotic range. The asymptotic convergence ratio of GCI32/(rp·GCI21) ≈0.998 was close to a value of 1, denying the reliability of the net independence study. Considering the balance between high numerical accuracy and computational time efficiency, Intermediate-level nets (360,087 elements) were selected for the entire subsequent parametric simulation [13], [16].

Regulator Equations and Porous Evaporation Models

Computational Fluid Dynamics (CFD)-based simulations solve the equations of mass conservation (continuity), momentum (Navier-Stokes), thermal energy, and species transport [23], [24]. The porous bearing effect is represented by the addition of hydrodynamic momentum (Si) source quarters using the Darcy-Forchheimer approach [25], [26], which is formulated in Equation:

$$S_i = -\left(\sum_{j=1}^{3} D_{ij}\, \mu v_j + \sum_{j=1}^{3} C_{ij} \frac{1}{2} \rho |v| v_j\right) \tag{3}$$

where Dij is the matrix of viscose resistance coefficient (1/α), Cij is the matrix of inertial resistance coefficient (C2), μ is the dynamic viscosity of air (1.82×10−5 Pa·s), ρ is the density of air (1,200 kg/m3), and v is the surface velocity (1.0 m/s).

The internal flow regime in the pore matrix is evaluated using the *Pore Reynolds Number* (Repori) based on average pore/fiber diameter (dp=0.5 mm), which is formulated in Equation (2):

$$\mathrm{Re_{pori}} = \frac{\rho \cdot \mathrm{v} \cdot \mathrm{d_p}}{\mu} \tag{4}$$

At an input speed of 1.0 m/s, an exact value of Repori=32.97 is obtained. Due to Repori<100, this quantitatively confirms that the flow is in the domain of the dominance of the viscous regime (Darcy). Nevertheless, the inertial effect (Forchheimer) is maintained in the solver to maintain numerical continuity.

Based on the calculation of the pressure drop gradient (ΔP≈0.172 Pa at a thickness of 100 mm), the quantitative values of the coefficient of the main viscose resistance (1/αx) and the main inertial resistance (C2.x) were set at 8.95×104 m−2 and 0.15 m−1, respectively. In order to model the anisotropic character and prevent the penetration of abnormal flow in the lateral direction (y and z), the components of the transverse resistance matrix are set 100 times higher, resulting in the following anisotropic resistance matrices D and C:

$$\mathrm{D} = \begin{bmatrix} 8{,}95 \times 10^4 & 0 & 0 \\ 0 & 8{,}95 \times 10^6 & 0 \\ 0 & 0 & 8{,}95 \times 10^6 \end{bmatrix} \mathrm{m}^{-2} \tag{5}$$

$$C = \begin{bmatrix} 0{,}15 & 0 & 0 \\ 0 & 15{,}00 & 0 \\ 0 & 0 & 15{,}00 \end{bmatrix} m^{-1} \tag{6}$$

The fully wetted homogeneous assumption is applied, whereby the surface of the solids is assumed to be coated with a thin film of water at constant temperature... (the mass source term equation Sm and so on follow the new press numbering). The phase exchange is injected into the solver by adding the mass source term (Sm) to the water vapor species equation (H2O) and the latent energy source (Sh) term to the energy equation. The explicit form of the mass source term Sm(kg/m3·s) is formulated in Equation:

$$\mathrm{S_m} = \mathrm{a_v} \cdot \frac{\mathrm{k_m M_w}}{(\mathrm{RT})\left(\mathrm{P_{sat(T)}} - \mathrm{P_v}\right)} \tag{7}$$

where AV is the macroscopic specific surface area of the bearing set to 250 m2/m3, KM is the coefficient of convective mass displacement (m/s), Mw is the molar mass of water (0.018015 kg/mol), R is the ideal gas constant (8.314 J/mol·K), T is the local temperature (K), and Pv is the local water vapor partial pressure (Pa). The saturated vapor pressure as a function of local temperature, Psat(T) (Pa), is calculated using the Tetens correlation in Equation:

$$\mathrm{P_{sat(T)}} = 610{,}78 \times \exp\left(\frac{17{,}27 \cdot (\mathrm{T} - 273{,}15)}{\mathrm{T} - 35{,}85}\right) \tag{8}$$

The term of the latent energy source is defined as Sh=Sm·hfg, where hfg is the latent heat of water evaporation (2.44×106 J/kg). The source tribes Sm and Sh are dynamically injected into the ANSYS Fluent porous zone domain using a macro DEFINE_SOURCE macro-structured C-code User-Defined Function (UDF) program hooked directly into the Cell Zone Conditions → Source Terms menu. [23], [35].

Numerical Scenarios, Solver, and Validation

The flow parameters are represented by wet inlet air with a dry spherical (Tin) temperature of 21.0∘C (294.15 K), a velocity of 1.0 m/s, a relative humidity (RH) of 79.2%, and a humidity/moisture content ratio (w) of 0.0124 kg H2O/kg of dry air at an operating pressure of 1.0 atm (101.325 Pa). In order to guarantee the transparency and reproducibility of computational modelling, quantitative details of the thermophysical properties of the fluid phase (air-water vapor mixture) along with the thermodynamic operating conditions and their reference sources are presented separately in Table 3.

Table 3. Thermophysical Properties of Fluid Phase (Air-Water) and Operating Conditions of CFD Modeling

Thermophysical Parameters of Fluids	Symbols	Quantitative Value	Units	Test Operation Conditions (T,RH,P)	Sources / Literature References
Inlet Air Temperature	Tin	21,0 (294,15)	∘C (K)	P=1.0 atm	Operating Limit Conditions
Relative Moisture Intake	RHin	79,2	%	T=21.0∘C, P=1.0 atm	Operating Limit Conditions
Moisture Content/Moisture Ratio	w	0,0124	kg H2O/kgda	T=21.0∘C, RH=79.2%	ASHRAE Psychometry Table
Dry Air Density	ρair	1,200	kg/m3	T=21.0∘C, P=1.0 atm	ANSYS Fluent Database
Dynamic Viscosity of Air	μair	1.82×10−5	Pa·s	T=21.0∘C	ANSYS Fluent Database
Air Thermal Conductivity	Kair	0,0257	W/m·K	T=21.0∘C	ANSYS Fluent Database
Heat Type Air	cp,air	1006	J/kg·K	T=21.0∘C	Thermodynamics Standard
Latent Heat Water Evaporation	HFG	2.44×106	J/kg	T=21.0∘C	NIST WebBook/[23]
Molar Mass of Water	Mrs.	0,018015	kg/mol	Standard	IUPAC Standards/[23]
Ideal Gas Constant	R	8,314	J/mol·K	Standard	Physics Standards

The outlet boundary condition is set as a pressure outlet (0 Pa gauge), while the aisle wall is set as a no-slip adiabatic wall [13], [16]. The differential equation was solved using ANSYS Fluent software with the SIMPLE pressure-speed coupling algorithm and the Second-Order Upwind spatial dyskritisation scheme [16], [35]. The flow regime within the test aisle was first evaluated using a Reynolds number based on the aisle hydraulic diameter (Dh), which is formulated in Equation:

$$Re_{duct} = \frac{\rho \cdot v \cdot D_h}{\mu} \tag{9}$$

For the passage cross-section measuring 0.65 m wide and 1.83 m high, the hydraulic diameter was calculated as Dh=4A/P=0.9593 m. Under the inlet air condition (T=21∘C, ρ=1.200 kg/m3, μ=1.82×10−5 Pa·s) and a velocity v=1 m/s, Reduct≈63.250 was obtained. Since the Reduct value far exceeds the internal flow transition threshold (Re>4000), the use of turbulence modeling is fully theoretically justified.

The Realizable k−ε turbulence model combined with the Enhanced Wall Treatment scheme was chosen for its ability to accurately predict fluid diffusion and strain effects of flow across porous cross-sections [13], [16]. To ensure the reliability of near-wall integration, the feasibility of the mesh lattice was verified through quantification of the dimensionless value y+. The extraction results showed that the distribution of y+ was uniformly distributed across domains; In the adiabatic wall of the passageway, an average Y+ value of 0.82 (maximum 1.15) was obtained, while in the Pad boundary zone, an average Y+ value of 0.94 (maximum 1.38) was obtained. The consistency of the y+≤1 value confirms that the viscous sublayer is resolved accurately without relying on empirical wall functions. Strict convergence criteria were established: residual <10−6 for energy and species, <10−4 for other variables, as well as verification of global mass/energy flux imbalance below 1% [23], [35]. As a measure of verification of the reliability of the numerical model prior to the parametric iteration, the CFD setup was comprehensively validated (multiparameter) by comparing the response of temperature drop (ΔT), relative outflow humidity (RHout), pressure drop (ΔP), and evaporation rate of baseline computational results against experimental data of evaporative coolant from Almaneea et al. [4] at the air velocity range of 1 to 3 m/s. The level of computational accuracy was evaluated by quantitative using the Mean Absolute Percentage Error (MAPE) parameters in Equation (4) and Root Mean Square Error (RMSE) in Equation:

$$\mathrm{MAPE} = \frac{1}{n}\sum_{i=1}^{n}\left|\frac{\Delta T_{exp,i} - \Delta T_{CFD,i}}{\Delta T_{exp,i}}\right| \times 100\% \tag{10}$$

$$\mathrm{RMSE} = \sqrt{\frac{1}{n}\sum_{i=1}^{n}\left(\Delta T_{exp,i} - \Delta T_{CFD,i}\right)^2} \tag{11}$$

The results of qualitative and quantitative comparisons are presented in Table 3. The increase in air velocity from 1 m/s to 3 m/s shows a consistent trend of thermofluid variable change between the experimental data and numerical simulations. Error evaluation showed a high level of accuracy across the response parameters, with MAPE values of 4.38% (RMSE=0.161∘C) for ΔT, 0.28% (RMSE=0.22%) for RHout, 4.36% (RMSE=0.035 Pa) for ΔP, and 4.70% (RMSE=0.002 g/s) for evaporation rate, respectively. Since all MAPE values are well below the scientific feasibility tolerance threshold (<10%), *numerical* setups, porous barrier matrices, and evaporation source quarts have proven to be valid and reliable for use in the next stage of parametric simulation.

Table 4. Comparison of multiparameter validation (ΔT, RHout, ΔP, and Evaporation Rate) between the experimental data of Almaneea et al. [4] and the baseline CFD simulation at a velocity variation of 1–3 m/s.

Response Parameters	Speed, v(m/s)	Experiments [4]	CFD Baseline	Relative Error (%)	Eligibility Evaluation Metrics
Temperature Drop, ΔT (∘C)	1,0	4,20	4,05	3,57%	MAPE = 4.38% RMSE = 0.161 °C
	2,0	3,80	3,62	4,74%	
	3,0	3,10	2,95	4,84%	
Relative Humidity, RHout(%)	1,0	79,80	79,53	0,34%	MAPE = 0.28% RMSE = 0.22%
	2,0	79,60	79,38	0,28%	
	3,0	79,40	79,22	0,23%	
Pressure Drop, ΔP(Pa)	1,0	0,180	0,173	3,89%	MAPE = 4.36% RMSE = 0.035 Pa
	2,0	0,520	0,498	4,23%	
	3,0	1,050	0,998	4,95%	
Evaporation Rate (g/s)	1,0	0,029	0,028	3,45%	MAPE = 4.70% RMSE = 0.002 g/s
	2,0	0,042	0,040	4,76%	
	3,0	0,051	0,048	5,88%	

Experimental Design and Taguchi L9 Matrix

To map the influence of composite thermophysical architecture on performance, the Taguchi L9 orthogonal matrix method (3^3) is used [20]. The three parameters studied bulk density, effective porosity, and effective thermal conductivity were hypothetically obtained from the mechanical characterization range of pure PALF composite literature [11], [12].

Table 5. Orthogonal Matrix L9 Thermophysical Parameters

Scenario (Run)	Density (kg/m^3)	Porosity	K-thermal (W/m·K)
S1	810.3 (L1)	0.8595 (L1)	0.0361 (L1)
S2	810.3 (L1)	0.9197 (L2)	0.0425 (L2)
S3	810.3 (L1)	0.9800 (L3)	0.0489 (L3)
S4	953.3 (L2)	0.8595 (L1)	0.0425 (L2)
S5	953.3 (L2)	0.9197 (L2)	0.0489 (L3)
S6	953.3 (L2)	0.9800 (L3)	0.0361 (L1)
S7	1096.3 (L3)	0.8595 (L1)	0.0489 (L3)
S8	1096.3 (L3)	0.9197 (L2)	0.0361 (L1)
S9	1096.3 (L3)	0.9800 (L3)	0.0425 (L2)

The thermofluid performance of a cooling system is evaluated through three main indicators: temperature drop (ΔT=Tin−Tout), static pressure loss (ΔP=Pin−Pout), and wet ball effectiveness (ε). Wet ball effectiveness (ε) evaluates the extent to which actual cooling is close to the theoretical limit of cooling potential, which is explicitly formulated in Equations (2) [3], [4]:

$$\varepsilon = \frac{T_{in} - T_{out}}{T_{in} - T_{wb}} \times 100\% \tag{12}$$

where Tin is the temperature of the inlet air dry ball (21.00∘C), Tout is the average mass of the air-dry ball temperature (∘C), and Twb is the wet ball temperature of the inlet air (∘C).

The value of Twb was calculated precisely based on the psychometric conditions of the incoming air (Tin=21.0∘C and RH=79.2%) using Stull's empirical formulation in Equation (3) [36]:

$$T_{wb} = T_{in} \cdot \arctan\left(0{,}151977(RH + 8{,}313659)^{\frac{1}{2}}\right) + \arctan(T_{in} + RH) \tag{13}$$

where the trigonometric function of arctan is evaluated in radians [36]. The substitution of the inlet boundary condition (Tin=21.0∘C, RH=79.2%) into Equation (3) results in an exact wet ball temperature value of Twb=18.39∘C, which gives a maximum wet ball depression limit of ΔTmax=Tin−Twb=2.61∘C.

Sensitivity analysis was performed on the ΔT response variable using a Signal-to-Noise (S/N) ratio of the Larger-the-Better type expressed with the equation:

$$\frac{S}{N} = -10 \log_{10}\left(\frac{1}{n}\sum_{i=1}^{n}\frac{1}{y_i^2}\right) \tag{14}$$

Since CFD calculations are deterministic and have no fluctuations (external noise factors), the S/N equation essentially operates as a response logarithmic transformation [20]. The rating is based on the magnitude of the main effect (maximum S/N delta value), which is re-verified through confirmation simulations.

RESULTS

Recapitulation of Simulation Results and Thermodynamic Performance

The implementation of the Computational Fluid Dynamics (CFD) simulation on nine combinations of Taguchi L9 matrices resulted in the variation in airflow response and evaporative cooling shown in Table 1. To evaluate the thermodynamic reliability, the inlet air temperature (Tin) was pegged at a constant at 21,000∘C (294.150 K) with an inlet relative humidity (RH) of 79.20%. Based on psychometric properties, the theoretical cooling limit (wet-bulb temperature, Twb) under these conditions is approximately 18.39∘C, so the maximum wet-bulb depression potential is ≈2.61∘C. All outputs in Table 1 were taken using the mass-weighted average method precisely at the bearing output plane (100 mm thickness), to ensure that there was no bypass effect of the external airflow that cluttered the data. The mass and energy balance imbalance (mismatch) in all scenarios was recorded below the 1% numerical tolerance range.

Table 6. Recapitulation of thermofluid simulation results in L9 scheme (Inlet air: 21,000�C, RH 79.20%, 1 m/s)

Scenario	Density (kg/m^3)	Porosity	K-thermal (W/m·K)	All(°C)	ΔT(°C)	ΔP(Pa)	Effectiveness (%)	RHout(%)	Evaporation Rate (g/s)
S1	810,3	0,8595	0,0361	20,926	0,074	0,173	2,827	79,53	0,028
S2	810,3	0,9198	0,0425	20,922	0,078	0,172	2,986	79,55	0,030
S3	810,3	0,9800	0,0489	20,946	0,054	0,172	2,067	79,44	0,020
S4	953,3	0,8595	0,0425	20,926	0,074	0,172	2,833	79,53	0,028
S5	953,3	0,9198	0,0489	20,853	0,147	0,172	5,627	79,88	0,056
S6	953,3	0,9800	0,0361	20,946	0,054	0,172	2,067	79,44	0,020
S7	1096,3	0,8595	0,0489	20,926	0,074	0,172	2,833	79,53	0,028
S8	1096,3	0,9198	0,0361	20,938	0,062	0,172	2,373	79,48	0,023
S9	1096,3	0,9800	0,0425	20,912	0,088	0,172	3,386	79,61	0,033

Of the nine tests, Scenario 5 (S5) recorded a maximum temperature drop of 0.147∘C with the highest evaporation effectiveness in the observation matrix of 5.627%. The static pressure loss (ΔP) that crosses the porous zone ranges from a very narrow margin, i.e., 0.1718–0.1728 Pa. This very light ΔP value is a logical consequence of the high macroscopic porosity ratio (0.85–0.98) and the slow input flow rate (1 m/s), where the viscose resistance has not been significantly amplified. Meanwhile, the relatively small absolute ΔT value compared to the theoretical wet spherical depression indicates that the latent heat exchange rate (represented by an evaporation rate of 0.020–0.056 g/s) in this PALF composite thermophysical model is still operating at a slow diffusion rate when compared to conventional cellulose pads.

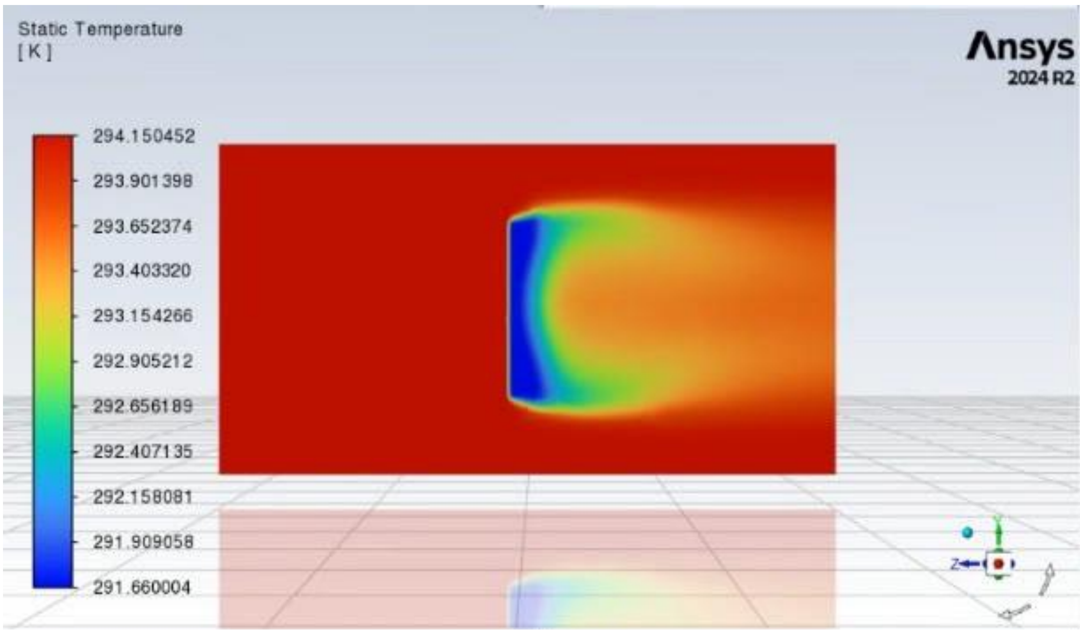

Figure 2. The spatial distribution contour of the static temperature in the mid-plane across the porous zone of the cooling pad.

Visual analysis of the spatial distribution (Figure 2) clarifies the thermofluid transport mechanism around the bearing. The *mid-plane* plane shows that the temperature profile undergoes cooling stratification just after air crosses the bearing thickness, synchronous with the projected increase in relative humidity (RH) contours on the *outlet side*. The pressure decrease is characterized by a thin positive pressure resistance zone upstream of the bearing, while the velocity contour validates the homogeneity of perpendicular air penetration through the pore matrix without adverse bypass turbulence fluctuations.

Ranking of Influence Factors Based on S/N Ratio and Variance Analysis (ANOVA)

Examination of the average response value showed that the air cavity ratio (porosity) presented the most dramatic fluctuations in thermofluid performance compared to solids density and thermal conductivity. Larger-the-better type Signal-to-Noise (S/N) ratio analysis was applied to the ΔT metric. Given that CFD simulations are deterministic without external random fluctuations (noise factors), the S/N equation operates as a qualitative logarithmic transform to clarify the main effect. Table 7 presents the results of factor ranking based on the S/N delta difference.

Table 7. Factor ranking for ΔT response based on S/N ratio

Material Parameters	Level 1 (dB)	Level 2 (dB)	Level 3 (dB)	Difference (Delta)	Influence Ranking
Porosity (φ)	-22,621	-20,988	-23,923	2,935	1
Thermal Conductivity (k)	-24,045	-21,946	-21,540	2,505	2
Density of Solids (ρsolid)	-23,381	-21,540	-22,611	1,840	3

To strengthen the statistical validation and quantify the relative contribution of each thermophysical parameter to the variability of temperature drop (ΔT), Variance Analysis (ANOVA) was performed [18]–[20]. The sum of squares (SS), degrees of freedom (df), mean square (MS), F-value, and percentage contribution (% Contribution) are formulated in Equations (4) and (5):

$$SS_{faktor} = n_{level} \sum_{j=1}^{3} (\bar{y}_j - \bar{y}_{global})^2 \quad (12)$$

$$\% \text{ Contribution} = \left(\frac{SS_{faktor}}{SS_{total}}\right) \times 100\% \quad (13)$$

The results of the ANOVA calculation are presented in detail in Table 8.

Table 8. Analysis of Variance (ANOVA) and Percentage Contribution Factors to ΔT Response

Source of Variance	**Degree of Freedom (df)**	**Number of Squares (SS)**	**Squared Average (MS)**	**F-Value**	**Percentage of Contribution (% *Contribution*)**
Porosity (φ)	2	0,001465	0,000732	0,527	23,19%
Thermal Conductivity (k)	2	0,001217	0,000608	0,438	19,26%
Density of Solids (ρsolid)	2	0,000854	0,000427	0,307	13,52%
Residual *Error*	2	0,002781	0,001390	-	44,03%
Total	8	0,006316	-	-	100,00%

Table 8 quantitatively confirms that Porosity (φ) provides the dominant contribution percentage of 23.19% to temperature decrease variations, followed by Thermal Conductivity (19.26%) and Density of Solids (13.52%). ANOVA's findings are fully consistent with the S/N ratio ranking hierarchy in Table 7.

Analysis of the Effects of Inter-Factor Interactions

Methodologically, the Taguchi L9(3 3) orthogonal design allocates all the main 6df (2×3 factors) to isolate the independent effects of Porosity, Thermal Conductivity, and Density of Solids. Due to the degree of freedom limitation in the L9 matrix, the effects of two-factor interactions (such as φ×k or φ×ρsolid) that require 4df per interaction pair are mathematically confound and absorbed into the residual error/error (residual error, SSError=44.03%) [19], [20]. Although not isolated separately in the statistical table, the inter-parameter interactions were evaluated phenomenologically through combined thermofluid responses. The peak of temperature drops (ΔT=0.147∘C at S5) indicated a strong synergistic interaction between mid-level porosity (φ=0.9198) and high-level thermal conductivity (k=0.0489 W/m·K). Intermediate porosity provides a balance of air cavity volume and water contact interface area, while high thermal conductivity accelerates the supply of internal conduction heat to the water film, thereby triggering a maximum latent evaporation rate [15], [28]. In contrast, if the porosity is raised to an extreme level (φ=0.9800), the increase in thermal conductivity no longer has a significant cooling impact due to the dispersion of the water-absorbing solid matrix [17], [27].

Trends at the factor level indicate that the energy exchange efficiency peaks at the intermediate level of the tested matrix (Porosity 0.9198, Density of Solids 953.3 kg/m^3, and Thermal Conductivity 0.0489 W/m·K). This is in line with the theory of pore mechanics; excessively high porosity leads to a reduction in the specific surface area of water availability resulting in a decrease in mass transfer, while excess density triggers microscopic blockages that narrow the phase diffusion contact time [17], [27]. In contrast, thermal conductivity is directly proportional, where the highest conductivity value (0.0489 W/m·K) stimulates the smooth supply of conductive heat to maintain the continuity of homogeneous surface latent heat extraction [15], [28].

Based on the main effect S/N, the optimal numerical parameter combination is predicted to be at the level A2-B2-C3 (Density Level 2, Porosity Level 2, K-thermal Level 3). Coincidentally, this predictive array is identical to Scenario 5 (S5) on the orthogonal matrix. Verification of computational confirmation demonstrates a prediction error between parameters close to 0%, eliminating S5 as the top numerical configuration array within the constraints of this experimental matrix.

Although S5 presents the best heatflow equilibrium point, the still limited maximum ΔT findings confirm that the application of polymer-PALF composite mechanical data requires further optimization of the interface physics. Therefore, this architectural recommendation stands firmly as a thermofluid sensitivity benchmark model, underscoring the need for physical experimental validation of real PALF pads before they are universally claimed as a substitute for conventional pads.

DISCUSSION

Performance Characteristics and Practical Significance of Thermofluids

The simulation findings show that the highest cooling effectiveness achieved in this experimental matrix is only around 5.627% with a maximum temperature drop (ΔT) of 0.147∘C. In practical terms, this figure is very low when compared to commercial evaporative cooling pads made of corrugated cellulose, which are generally capable of achieving 50%–80% effectiveness in the speed range of 1–3 m/s [3], [33]. This moderate numerical performance can be explained by two main limiting factors: thermodynamic conditions and limitations of model formulation.

First, the simulation was run under conditions of very high humidity (RH 79.20%, Tin21∘C). In the psychometrics of direct evaporative cooling systems, the absolute cooling limit is not determined by the dew point temperature, but by the wet-bulb temperature of the incoming air [4], [34]. The initial high RH causes the incoming air to be close to saturation, so that the wet ball depression that facilitates evaporation (the difference between dry and wet bulb) becomes very narrow (≈2.61∘C). This fundamentally limits the latent heat exchange capacity of air-water, regardless of the type of material used [3], [4].

Second, the thermophysical parameters of PALF-derived composites are applied into the macroscopic CFD model without directly modifying the micro-capillarity interactions or real phase dynamics (wettability). The resulting pressure loss value (ΔP) is also very small (≈0.17 Pa), indicating that the homogeneous porosity structure inputted into the software provides very weak hydrodynamic resistance at a speed of 1 m/s [25], [30]. This condition may pass the airflow (short residence time) before the transfer of water vapor mass occurs optimally.

Interpretation of Causality of Thermophysical Factors (Density, Porosity, and Thermal Conductivity)

In the design of the Taguchi L9 Matrix, all three factors were tested mathematically independently. The results of the S/N analysis showed that the fluctuations in air resistance (ΔP) between levels were very marginal (0.1718–0.1721 Pa), where the average ΔP at the lowest density was slightly higher [8]. This confirms that within the limitations of this macroscopic model, the increase in the density value of the composite matrix affects the thermal inertia capacity of the solid phase, without automatically changing the volume of the cavity or structurally "clogging" the pores (given that porosity is regulated as a standalone factor). Thus, the small variation in the aerodynamic profile is more of a numerical response to changes in the empirical coefficient of diffusion and the resistance matrix in the software, rather than evidence of a change in the physical structure of the material.

Among the three factors, porosity appears to be the most dominant macro parameter controlling the thermal response. Optimum performance is achieved at the intermediate level porosity (0.9198), not at the highest level (0.9800). Hypothetically based on the theory of heat transfer of porous media, excessively high porosity causes the proportion of the volume of the moisture-storing solid matrix to be too minor [17], [27]. In the formulation of the source term of the CFD mass displacement, the reduction in solid volume can be directly proportional to the shrinkage of the macroscopic specific surface area (although in this study it is assumed to be uniformly fully wetted) [23], [35]. As a result, the intermediate porosity ratio is hypothesized to present the best balance between the air circulation passage and the wide availability of thermofluid contact interfaces [3], [4].

Meanwhile, an increase in thermal conductivity is effective in showing a positive trend towards cooling effectiveness. Although traditional studies often use high-insulating cellulose [6], conductivity modifications in composites (e.g. up to 0.0489 W/m·K) are believed to help accelerate the transmission of local heat in the solid fibers to the water film interface, ensuring that evaporation energy is not only dependent on the convection of the air boundary, but also an adequate supply of internal conduction propagation of the material [15], [28].

To ensure that the observed variation in cooling performance in the Taguchi matrix is a physical phenomenon due to the response of the material's thermophysical properties and not a numerical uncertainty error, a comparative evaluation was performed on the mesh convergence error. Based on the mesh independence analysis, the difference in output temperature (Tout) between the coarse mesh and the medium/fine mesh resulted in a convergence error of 0.044∘C. On the other hand, the maximum deviation of temperature drop between simulation scenarios recorded a value of Δ(ΔT)=0.093∘C (i.e. the difference between the highest response in S5 of 0.147∘C and the lowest response in S3/S6 of 0.054∘C). The ratio between the inter-scenario deviations to net independence errors exceeding a factor of two (Δ(ΔT)/Errormesh≈2.11) critically proves that the resulting thermofluid response differences have valid numerical significance and are above the threshold of computational net uncertainty.

Limitations of Modeling

Several assumptions accompany the limitations of these computational studies. Porous zone modeling was performed in a homogeneous-isotropic manner, in which in fact the structure of PALF composite fibers is anisotropic with a complex particle orientation [5], [9]. The steady-state assumption of fully *wetted* ignores the phenomenon of water distribution dynamics dependent on the supply pump rate, the thickness of the liquid film layer, the viscosity of the thermal fluid, and the capillarity of natural fibers [23], [35]. Furthermore, the simulation is fixed on a set of thermodynamic boundary parameters of flow velocity, T, and RH, and the experimental design design does not explore cross-interactions between factors. The S/N influence rating is an internal numerical sensitivity analysis and has not been verified for accuracy through physical prototyping under wind tunnel testing conditions.

CONCLUSION

This numerical study evaluated the thermophysical sensitivity of pineapple leaf fiber-based composites (PALF) to thermofluid performance under a single humid inlet air restriction scenario (21∘C, RH 79.2%, and velocity of 1 m/s). Based on the Signal-to-Noise (S/N) ΔT rating analysis, porosity showed the highest level of numerical sensitivity, followed by thermal conductivity and density. Among the nine matrix scenarios tested, the combination of S5 (equivalent to the Taguchi level A2-B2-C3: porosity 0.9198, solids density 953.3 kg/m^3, and thermal conductivity 0.0489 W/m·K) was predicted to be the best composition. At the single operating point, this combination resulted in a temperature drop (ΔT) of 0.147 °C, a cooling effectiveness of 5.627%, and a pressure drop (ΔP) of 0.172 Pa. These computational results are specific and apply only to the range of pore architecture level and thermodynamic conditions evaluated. The moderate performance confirms the fundamental limitations on direct evaporative cooling due to the narrowing potential for wet ball depression in humid environments. Therefore, these results purely serve as a basic hypothesis for the selection of numerical parameters for the design, not as proof that these composite materials are high-performance or ready to replace conventional cellulose pads. To follow up on this design potential, future research agendas must prioritize thermal-hydraulic experimental validation, including source term verification of evaporation, measurement of actual evaporation rate (RH), water uptake capacity, and actual pressure resistance testing on closed duct prototypes without bypass flows. Furthermore, comprehensive evaluation mapping of various psychometric conditions and airflow velocity, testing of pump/fan power requirements, wet mechanical strength, resistance to wet-dry cycles (aging), biofouling, and fungal growth are crucial before the feasibility of commercial applications of this natural material can be concluded.

REFERENCES

[1] Y. Ding et al., "Emerging Engineered Wood for Building Applications," Chemical Reviews, vol. 123, no. 5, pp. 1843–1888, 2022.
[2] H.-L. Lou and S. Hsieh, "Towards Zero: A Review on Strategies in Achieving Net-Zero-Energy and Net-Zero-Carbon Buildings," Sustainability, vol. 16, no. 11, p. 4735, 2024.
[3] D. P. Patel, S. K. Jain, S. S. Lakhawat, and N. Wadhawan, "A low-cost storage for horticultural commodities for enhancing farmer's income: An overview on evaporative cooling," Journal of Food Process Engineering, vol. 45, no. 10, 2022.
[4] A. Almaneea et al., "Experimental investigation of air cooler using local palm tree waste," Heliyon, vol. 8, no. 8, p. e10265, 2022.
[5] M. A. Hidalgo-Salazar et al., "Colombian natural fibers: Potential applications in sustainable natural fiber reinforced composites materials," Polymer Composites, vol. 46, no. 6, pp. 5599–5617, 2024.
[6] B. Klemczak, B. Kucharczyk-Brus, A. Sulimowska-Ociepka, and R. Radziewicz-Winnicki, "Historical Evolution and Current Developments in Building Thermal Insulation Materials A Review," Energies, vol. 17, no. 22, p. 5535, 2024.
[7] R. Venkataswamy et al., "Environmental Impact Assessment of Chemical Mechanical Planarization Consumables: Challenges, Future Needs, and Perspectives," ACS Sustainable Chemistry & Engineering, vol. 12, no. 32, pp. 11841–11855, 2024.
[8] T. Amornsakchai and S. Duangsuwan, "Upcycling of HDPE Milk Bottles into High-Stiffness, High-HDT Composites with Pineapple Leaf Waste Materials," Polymers, vol. 15, no. 24, p. 4697, 2023.
[9] S. de S. Barros et al., "Extraction of cellulose nanofibrils and nanocrystals from a new cultivar of pineapple (Ananas comosus 'Vitória') from the Amazon region," Biofuels, Bioproducts and Biorefining, 2025.
[10] A. Rukundo, P. M. Dass, and N. I.I., "Study of Extraction, Treatment and Characterization of Pineapple Leaves Fibers as Potential Utility in Textile Industry," IDOSR Journal of Experimental Sciences, vol. 10, no. 2, pp. 60–76, 2024.
[11] T. Amornsakchai, S. Duangsuwan, K. Mougin, and K. L. Goh, "Comparative Study of Flax and Pineapple Leaf Fiber Reinforced Poly(butylene succinate): Effect of Fiber Content on Mechanical Properties," Polymers, vol. 15, no. 18, p. 3691, 2023.
[12] M. M. Sayeed et al., "Assessing Mechanical Properties of Jute, Kenaf, and Pineapple Leaf Fiber-Reinforced Polypropylene Composites: Experiment and Modelling," Polymers, vol. 15, no. 4, p. 830, 2023.
[13] A. Al-damook, S. A. Hafedh, F. S. Alkasmoul, I. D. J. Azzawi, and W. H. Khalil, "CFD-Enabled Design Optimization of

Natural Convection and Entropy Generation in a Porous Quarter-Circular Cavity," Heat Transfer, vol. 54, no. 6, pp. 3843–3861, 2025.
[14] S. Piedra, A. Gómez-Ortega, and J. Pérez-Barrera, "Prediction of Flow Properties of Porous Triply Periodic Minimal Surface (TPMS) Structures," Fluids, vol. 8, no. 12, p. 312, 2023.
[15] Y. Du, Q. Xu, C. Li, and C. Wang, "Synergistic effect of mixed wettability of micro-nano porous surface on boiling heat transfer enhancement," Thermal Science and Engineering Progress, vol. 42, p. 101933, 2023.
[16] S.-J. Li, L. Zhu, X. Zhang, and Z. Luo, "Recent Advances in CFD Simulations of Multiphase Flow Processes with Phase Change," Industrial & Engineering Chemistry Research, vol. 62, no. 28, pp. 10729–10786, 2023.
[17] I. Rusdianto, F. D. Ikram, W. Sarwana, and A. Hidayat, "Effect of Composition of Sugarcane Stalks, Rice Husk Ash and Polyester Resin on Thermal Conductivity and Sound Absorption," Journal of GEAR Energy Design Manufacturing & Materials, vol. 1, no. 2, pp. 101–108, 2023.
[18] O. Keklikçioğlu and V. Özceyhan, "Optimization of the Effects of Binary Hybrid Nanofluid Synthesis Parameters on the Thermal and Hydraulic Characteristics," Energy Environment & Storage, vol. 3, no. 2, pp. 59–65, 2023.
[19] A. Nurrohmad, Q. Antares, A. R. Nuranto, and A. Nugroho, "Optimization of Double Hole Composite Plate on the Floater Compartment of Amphibious Aircraft Using Taguchi Method," Warta Ardhia, vol. 49, no. 2, pp. 87–95, 2024.
[20] M. Oymak et al., "Parameter Sensitivity Analysis for Machining Operation of Autofrettaged Cylinder Using Taguchi Method," Applied Sciences, vol. 14, no. 13, p. 5523, 2024.
[21] Y. Hu, H. Zhao, W. Shi, C.-W. Bi, and X. Li, "Numerical Study on Internal and External Flow Fields of the UHMWPE Cage," Journal of Marine Science and Engineering, vol. 11, no. 10, p. 1881, 2023.
[22] J. Zhang, J. Wang, Q. Yang, and Q. S. Li, "Simulation of Piston Effects on Platform Screen Doors Considering Air Leakage," Atmosphere, vol. 13, no. 12, p. 1967, 2022.
[23] K. Deore, N. P. Salunke, S. B. Pawar, Y. Pathak, and J. Khatik, "Performance modeling of fin-enhanced phase change material solar stills using MATLAB: A numerical approach," Environmental Progress & Sustainable Energy, vol. 45, no. 1, 2025.
[24] M. Sosnowski et al., "Heat and Mass Transfer Analysis Within a Disc Shaped Fluidized Sorption Reactor," in 36th International Conference on Efficiency, Cost, Optimization, Simulation and Environmental Impact of Energy Systems, ECOS 2023, pp. 460-469, 2023.
[25] Y. Marykovskiy, G. Pomaranzi, P. Schito, and A. Zasso, "A Method to Evaluate Forchheimer Resistance Coefficients for Permeable Screens and Air Louvers Modelled as a Porous Medium," Fluids, vol. 9, no. 7, p. 147, 2024.
[26] A. Punyaponchai, "DEVELOPMENT OF A BAGHOUSE FILTER CFD MODEL FOR EFFICIENT PARTICULATE REMOVAL IN AIR FILTRATION SYSTEMS," International Journal of Geomate, vol. 26, no. 113, 2024.
[27] Z. Gan, T. Chen, R. Zhang, and R. Zhang, "Study on the Performance Degradation of Membrane Electrode Assembly in Proton Exchange Membrane Fuel Cell Caused by Freeze–Thaw Cycles," Fuel Cells, vol. 24, no. 4, 2024.
[28] G. U. N. Tajalla, P. Andriansyah, I. T. Riyadi, M. L. N. Vadila, and A. D. Laksono, "Thermal Characteristics of Composite Materials Based on Polypropylene and Banana Stems," Journal of Media Engineering for the Development of Science and Engineering Applications, vol. 23, no. 1, pp. 41–49, 2024.
[29] M. Venkataraman, S. Sözcü, and J. Militký, "Radiative Heat Transfer Properties of Fiber–Aerogel Composites for Thermal Insulation," Gels, vol. 11, no. 7, p. 538, 2025.
[30] L. Chatellier, Y. L. Guer, C. Bellot, X. Casiot, and L. David, "Pressure Loss Modeling for Multi-Stage Obstacles in Pressurized Ducts," Energies, vol. 17, no. 14, p. 3505, 2024.
[31] L.-N. Zhao, B. Chen, X. Li, H. Wang, and Q. Li, "Improvement of Numerical Simulation for Melting of the Composite Phase-Change Material Based on the Comparison with Experiment," Energy Technology, vol. 13, no. 10, 2025.
[32] J. Kumar, V. Mishra, A. Kumar, and S. Negi, "Characterization of 3D printable Polyethylene Terephthalate Glycol composite filament reinforced with agricultural waste derived from pineapple plant," Journal of Reinforced Plastics and Composites, vol. 44, no. 23–24, pp. 2812–2824, 2024.
[33] C. Guo, Y. Li, X. Li, R. Bai, and C. Dong, "Design Selection Method of Exhaust Air Heat Recovery Type Indirect Evaporative Cooler," Sustainability, vol. 15, no. 9, p. 7371, 2023.
[34] R.-C. Kim, K.-R. Hong, J.-Y. Yang, and W.-C. Yang, "High-pressure die casting process optimization for improving shrinkage porosity and air entrainment in carburetor housing with aluminum alloy using Taguchi-based ProCAST simulation and MADM-based overall quality index," The International Journal of Advanced Manufacturing Technology, vol. 132, no. 1–2, pp. 893–906, 2024.
[35] R. Schwarze, Experimental and Numerical Modeling of Fluid Flow, 2022.
[36] R. Stull, "Wet-Bulb Temperature from Relative Humidity and Air Temperature," Journal of Applied Meteorology and Climatology, vol. 50, no. 11, pp. 2267–2269, 2011.)